Power Electronic Systems
Laboratory

© 2017 IEEE

IEEE Transactions on Industrial Electronics, Vol. 64, No. 12, pp. 9806-9814, December 2017

Cogging Torque Shape Optimization of an Integrated Generator for Electromechanical Energy Harvesting

M. Flankl,
A. Tüysüz,
J. W. Kolar

Personal use of this material is permitted. Permission from IEEE must be obtained for all other uses, in any current or future media, including reprinting/republishing this material for advertising or promotional purposes, creating new collective works, for resale or redistribution to servers or lists, or reuse of any copyrighted component of this work in other works.

Eidgenössische Technische Hochschule Zürich
Swiss Federal Institute of Technology Zurich

This is the author's version of an article that has been published in this journal. Changes were made to this version by the publisher prior to publication.
The final version of record is available at http://dx.doi.org/10.1109/TIE.2017.2733441

Cogging Torque Shape Optimization of an Integrated Generator for Electromechanical Energy Harvesting

Michael Flankl, *Student Member*, *IEEE*, Arda Tüysüz, *Member*, *IEEE*, and Johann W. Kolar, *Fellow Member*, *IEEE*

***Abstract*—In contrast to widely applied cogging torque (CT) or detent torque optimization methods, where well-known concepts for achieving a low-ripple torque as stator and/or rotor skewing are applied, this paper proposes an approach for shaping the stator geometry of a permanent-magnet (PM) synchronous machine, such that an arbitrary CT pattern can be obtained. This is achieved by an iterative algorithm, which adds sinusoidal air gap modulation components on an initial machine geometry. The CT profile is calculated using 2-D FEM simulations and iterations are repeated until the desired CT pattern is achieved.**

The proposed approach is applied to an application example, where an outrunner PM generator is integrated in an electromechanical energy harvester (EEH). For this application, the generator's CT is beneficially shaped towards a 4-pole sinusoidal pattern with an amplitude of 100 Nmm. The optimized CT of the PM generator is used to counteract the holding torque of the EEH, where a reduction in the start-up speed of the EEH by a factor of 4 is observed. Moreover, the presented CT shaping approach is extended beyond the EEH example to illustrate that the described method is also suitable for axially short machines, where skewing is not feasible.

***Index Terms*—cogging torque, detent torque, torque ripple, energy harvesting, non-contact generator, optimization.**

I. Introduction

ONE can grasp the importance of cogging torque (CT), detent torque and torque ripple optimization by exploring the vast amount of literature published on this topic. Most publications discussing this issue are on permanent-magnet synchronous machines (PMSMs) and brushless DC (BLDC) machines. Permanent-magnet (PM) width [1] and shape [2]–[5] are commonly used parameters for CT optimization. Electric machine designs that adapt the teeth/slot shape and width [6], [7], inserting dummy slots [8] as well as introducing compensation windings [9] are also discussed in literature. An additional degree of freedom is the skewing of the stator [10] and/or the rotor [11]–[15]. The motivation behind CT optimization is usually the goal of reducing noise and vibration [16], [17] due to minimizing the CT to a value close to zero for the whole rotational period.

Manuscript received Month 02, 2017; revised Month 05, 2017; accepted Month 06, 2017. All authors are with the Power Electronic Systems Laboratory, Swiss Federal Institute of Technology, Zurich, 8092, Switzerland (e-mail: flankl@lem.ee.ethz.ch)

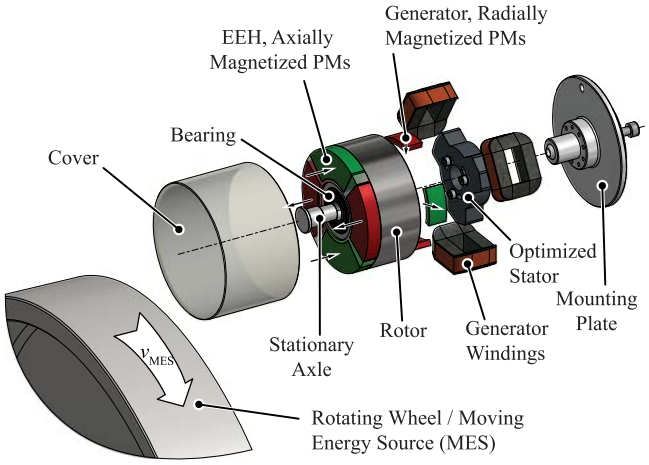

Fig. 1. Illustration of the electromechanical energy harvester (EEH) system. The generator, which exhibits an optimized CT pattern, is integrated in a pot shaped rotor.

On the other hand, methods for optimizing the CT towards a non-vanishing shape as shown for stepping motors [18] and DC machines in certain position-holding applications [19] are not as well established in literature. Both of above applications rely on the existence of a detent/holding torque, for achieving the angular positioning of the rotor without dissipating any losses in the machine windings.

Moreover, application-specific electric machines may also profit from a non-vanishing CT. For instance, generators that are directly coupled to a prime mover or machines directly coupled to a piston compressor may compensate the pulsating torque of the power source/load with a specially shaped CT. Accordingly, in such specific applications, the overall system performance could be improved with a specially shaped CT compared to targeting the pure minimization of CT in the individual electric machine.

A particular example of such a system, where an application-specific electric machine is directly coupled to a torque/mechanical power source, is the electromechanical energy harvester (EEH) shown in Fig. 1. In this arrangement, a set of axially magnetized PMs facing a rotating wheel made of an electrically conductive material forms a non-coaxial eddy-current coupling. Kinetic energy in the 10-watt range

Copyright (c) 2017 IEEE. Personal use is permitted. For any other purposes, permission must be obtained from the IEEE by emailing pubs-permissions@ieee.org.

This is the author's version of an article that has been published in this journal. Changes were made to this version by the publisher prior to publication.
The final version of record is available at http://dx.doi.org/10.1109/TIE.2017.2733441

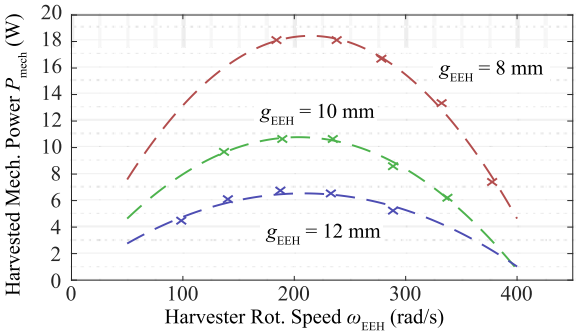

Fig. 2. Performance of the EEH, harvesting power from a steel wheel (moving energy source: MES) with $225\,\mathrm{mm}$ radius and a tip speed of $v_{\mathrm{MES}} = 22.2\,\mathrm{m/s}$. As the magnetic coupling decreases with larger air gaps g_{EEH}, a reduction in output power can be observed.

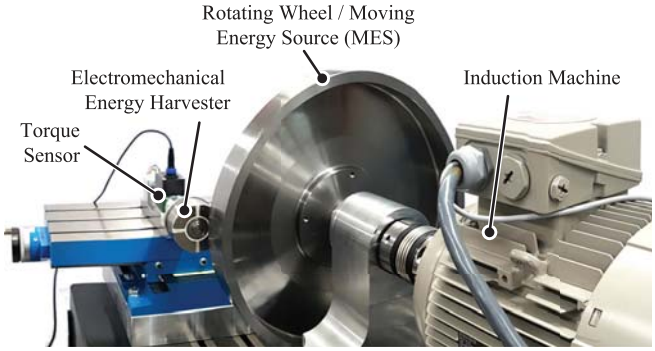

Fig. 3. In this setup, the CT of the EEH, which is facing the MES and the power output is measured. As it is shown in the photograph, the PMs of the EEH rotate to a position, such that the magnetic energy in the air gap between EEH and MES is minimized.

is harvested from the wheel [20] in a contactless manner and is converted into electrical energy by a generator integrated in the EEH.

The EEH can harvest energy from a wheel/surface made of a non-ferromagentic material such as aluminum, or a ferromagnetic material such as steel. However, due to the non-coaxial arrangement, the latter case results in a large CT $T_{\mathrm{cog,harv}}$, which limits the EEH's usability as detailed in Sec. II. For this, application specific highly relevant case, a compensation can be achieved when the generator features a CT $T_{\mathrm{cog,gen}}$ with same amplitude but opposite sign for all angular rotor positions θ [21]

$$\begin{aligned} T_{\mathrm{cog,gen}}(\theta) + T_{\mathrm{cog,harv}}(\theta) &\stackrel{!}{=} 0 \\ \Rightarrow T_{\mathrm{cog,gen}}(\theta) &= -T_{\mathrm{cog,harv}}(\theta)\ . \end{aligned} \tag{1}$$

In this paper, an algorithm that is capable of shaping an electric machine's CT towards a desired pattern is presented and the hardware implementation of such an optimized machine is detailed. Furthermore, measurement results verify the capability of the presented approach.

A detailed description of the application example at hand, the EEH, is given in Sec. II. The concept of air gap modulation for modifying the CT is analyzed in Sec. III-A. Then, Sec. III-B details the numeric optimization algorithm. Additionally, in Sec. IV, the proposed method is applied not only for achieving a desired CT profile, but also extended towards the design of a cogging-free machine design. Simulation results as well as experimental results from a hardware prototype are given in Sec. IV, and the clear benefit of the presented method in terms of lowering the start-up speed of the energy harvester is shown. Finally, Sec. V summarizes the main results of this paper.

II. Application Example: Electromechanical Energy Harvester

The EEH that was initially introduced in [20] comprises axially magnetized arc-segment-shaped PMs and a steel yoke. This assembly is free to rotate around its axis of rotation. When placed in the proximity of a rotating conductive body, which is henceforth denoted as moving energy source (MES), the eddy-current coupling results in a torque on the EEH. In [20], a MES made of aluminum is considered, and a BLDC machine is utilized as generator.

The axial-flux arrangement of the PMs increases the magnetic coupling between the EEH and the MES, compared to the radial-flux setup shown in [22]. On the other hand, this increased coupling also results in an increased CT applying on the EEH, when a MES made of ferromagnetic material, e.g. steel, is considered. This means that the eddy-current coupling needs to build up a high torque in order to initiate the EEH motion, and the harvesting of electrical energy. In other words, the start-up of the system is only possible at impractically high MES speeds, when the eddy-current coupling torque is larger than the peak value of the CT.

Fig. 2 shows measurement values for the harvested mechanical power at different rotational speeds of the EEH and different air gaps. The MES made of C45E steel (material No. 1.1191 [23]) is rotating with a constant tip speed of $v_{\mathrm{MES}} = 22.2\,\mathrm{m/s}$ in the provided measurement.

Finally, the harvested kinetic energy by said eddy-current coupling has to be converted in a generator into electric energy. In order to achieve a compact EEH unit, the EEH's generator is integrated as an outrunner in the pot-shaped EEH rotor (cf. Fig. 1).

A. System Start-up

It has to be noted that the CT and start-up issues are non-existing in an application with a non-ferromagnetic MES (e.g. made of aluminum) or a coaxial arrangement of EEH and MES. On the other hand, considering a ferromagnetic (e.g. steel) MES and a non-coaxial harvester arrangement will clearly broaden the possible application area of the EEH under consideration. Therefore, the resulting challenge of the start-up in the latter case is addressed in detail in this work.

Fig. 3 depicts the setup for measuring the EEH CT, and Fig. 4 shows the measurement results for different air gaps. A high precision rotational torque sensor with a measurement range of $\pm 200\,\mathrm{Nmm}$ and an accuracy of $\pm 0.2\,\mathrm{Nmm}$ was utilized.

Copyright (c) 2017 IEEE. Personal use is permitted. For any other purposes, permission must be obtained from the IEEE by emailing pubs-permissions@ieee.org.

This is the author's version of an article that has been published in this journal. Changes were made to this version by the publisher prior to publication.
The final version of record is available at http://dx.doi.org/10.1109/TIE.2017.2733441

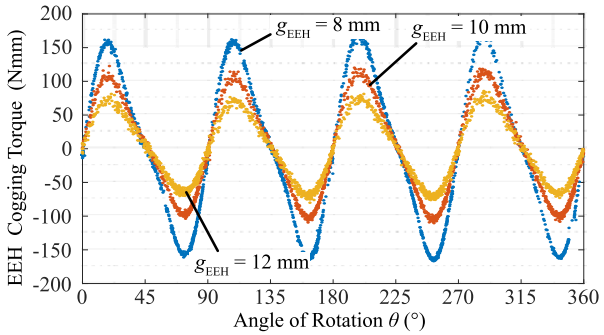

Fig. 4. CT measurements of the EEH shows an approximately sinusoidal pattern. The curve is repeated for every PM facing the MES and a strong dependency between amplitude and air gap can be observed.

In addition to the passive torque ripple minimization methods based on geometric modifications, current profiling has also been proposed in literature as an active method for the same effect [24]–[32]. This would, in principle, also be applicable to the energy harvester discussed here. The generator could operate in motor mode at the system start-up in order to overcome the EEH CT and to provide the initial motion. However, this would mean that the energy harvester is powered up from an energy storage. Therefore, this idea is not considered further.

B. Electromechanical Energy Harvester with Integrated Outrunner Generator

Since the EEH, which harvests kinetic power from the MES, has a disk-shaped geometry, a favorable mechanical design is accomplished if the generator is implemented as an outrunner in a pot-shaped extension of the EEH (cf. Fig. 1 and Fig. 5).

The axially magnetized EEH PMs and the radially magnetized generator PMs are mounted on a pot-shaped steel rotor. Different sets of PMs are used for the EEH and the generator, as this conveniently allows the decoupling of both magnetic designs. The rotor forms a magnetic yoke for all placed PMs and is machined out of a solid steel (S235) block. The stator, on the other hand, is made of laminated electrical steel M235-35A. As expressed in (1), the generator will be optimized such that its CT compensates the CT of the EEH (cf. Fig. 4).

The coils for a three phase winding with concentrated windings are wound on 3-D printed coil formers and placed on the stator's teeth.

III. Cogging Torque Optimization

In order to facilitate the understanding of the CT optimization algorithm shown in Sec. III-B, initially, the flux modulator depicted in Fig. 6 is considered. In order to compensate the CT of the EEH, a flux modulator with a CT of same mechanical period (90°) could be utilized. Originating from a symmetry analysis, the flux modulator must show the same number of magnets ($n_{\mathrm{PM}} = 4$) as the EEH.

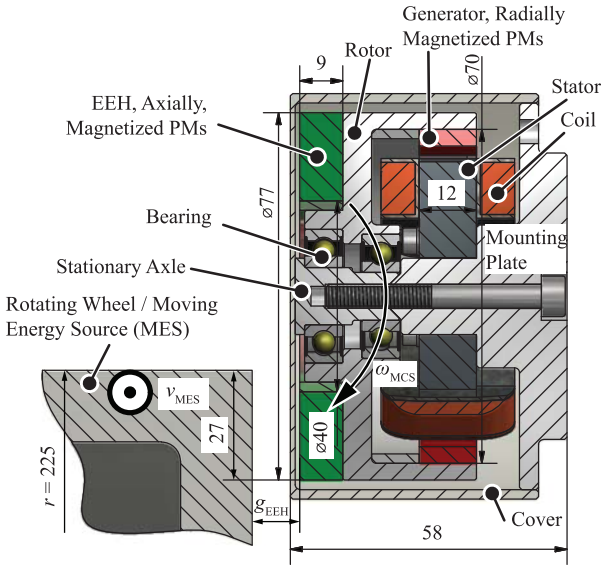

Fig. 5. Cross-section of the EEH, showing the compact arrangement of the EEH with integrated generator and the actual geometric dimensions of the hardware prototype (all dimensions in mm).

A. Cogging Torque of a Flux Modulator

Henceforth, for the flux modulator an air gap $g(\alpha)$ and a PM remanent flux density $B_{\mathrm{rem,r}}(\alpha, \theta)$ in the form of

$$g(\alpha) = g_0 \cdot (1 + m_{\mathrm{c},1} \cos(4\,\alpha)) \tag{2a}$$

$$B_{\mathrm{rem,r}}(\alpha, \theta) = B_{\mathrm{rem}} \cos(2\,(\alpha - \theta)) \tag{2b}$$

are assumed, where α is the geometric angle in the stator coordinate system.

By applying Ampere's law as described in [33]

$$\oint_S \frac{\vec{B}}{\mu} \mathrm{d}\vec{s} = \int_A \vec{j}\, \mathrm{d}\vec{A}\ , \tag{3}$$

on an arbitrary integration path including the stator, air gap, PMs and the rotor (one such path is indicated in Fig. 6), and by assuming $\mu_{\mathrm{Fe}} \to \infty$, $\mu_{\mathrm{PM}} = \mu_0$, the radial component of the air gap flux density can be calculated as

$$B_{\mathrm{r}}(\alpha, \theta) = \frac{B_{\mathrm{rem,r}}(\alpha, \theta)}{g(\alpha)/h_{\mathrm{m}} + 1}\ . \tag{4}$$

The total magnetic energy, which is only stored in the air gap and PMs, can then be calculated as

$$W_{\mathrm{m}}(\theta) = l_{\mathrm{y}} \int_0^{2\pi} \frac{B_{\mathrm{r}}^2(\alpha, \theta)}{2\,\mu_0} \cdot (h_{\mathrm{m}} + g(\alpha)) \cdot \underbrace{(d_1/2 - g(\alpha)/2)}_{r(\alpha)}\, \mathrm{d}\alpha\ , \tag{5}$$

where l_{y} is the axial length and h_{m} is the radial magnet height.

Finally, the CT acting on the rotor can be obtained as the derivative of the stored magnetic energy $W_{\mathrm{m}}(\theta)$ with respect to the angular position of the rotor θ,

$$T_{\mathrm{cog}}(\theta) = -\frac{\partial W_{\mathrm{m}}(\theta)}{\partial \theta} = k_{\mathrm{s},1} \sin(4\,\theta)\ , \tag{6}$$

Copyright (c) 2017 IEEE. Personal use is permitted. For any other purposes, permission must be obtained from the IEEE by emailing pubs-permissions@ieee.org.

This is the author's version of an article that has been published in this journal. Changes were made to this version by the publisher prior to publication.
The final version of record is available at http://dx.doi.org/10.1109/TIE.2017.2733441

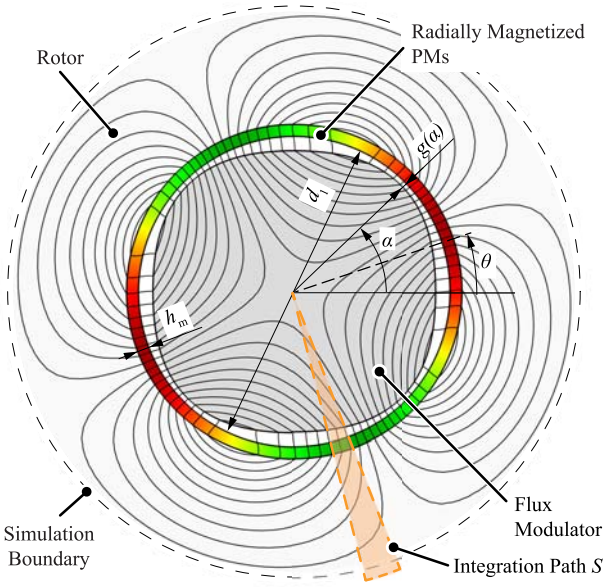

Fig. 6. Illustration of a flux modulator. Sinusoidal modulation of the air gap $g(\alpha)$ and magnetization $B_{\mathrm{rem,r}}(\alpha)$ are employed for shaping the CT towards the desired pattern.

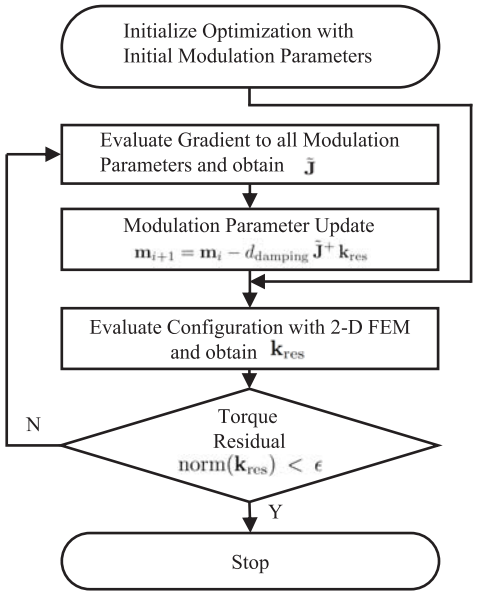

Fig. 7. Optimization algorithm flowchart. Starting from an initial geometry, the design is iterated by means of adapting the air gap modulation parameter vector $\mathbf{m}$, such that the optimization goal of $\mathbf{k}_{\mathrm{res}} < \epsilon = 5\,\mathrm{Nmm}$ is achieved.

where $k_{\mathrm{s},1}$ can be expressed as

$$k_{\mathrm{s},1} = l_{\mathrm{y}}\,\pi\,B_{\mathrm{r}}^2\,h_{\mathrm{m}}^2\,(d_1+h_{\mathrm{m}})\cdot \frac{g_0\,(\gamma+m_{\mathrm{c},1}-1)-h_{\mathrm{m}}\,(1-\gamma)}{\mu_0\,m_{\mathrm{c},1}\,g_0(g_0\,(1-m_{\mathrm{c},1})+h_{\mathrm{m}})}\,, \tag{7}$$

with

$$\gamma = \sqrt{1-\frac{2\,m_{\mathrm{c},1}}{1+m_{\mathrm{c},1}+{}^{h_{\mathrm{m}}}/_{g_0}}}\,.$$

Naturally, the air gap modulation can be extended by including additional terms

$$g(\alpha) = g_0\cdot(1+\sum_{i=1}^{n} m_{\mathrm{c},i}\,\cos(4\,i\,\alpha)+m_{\mathrm{s},i}\,\sin(4\,i\,\alpha)), \tag{8}$$

which will be the basis for geometry optimization in the following section. Accordingly, the CT is represented in the following as

$$T_{\mathrm{cog}}(\theta) = \sum_{i=1}^{n} k_{\mathrm{s},i}\,\sin(4\,i\,\theta)+k_{\mathrm{c},i}\,\cos(4\,i\,\theta)\,. \tag{9}$$

Furthermore, the modulation parameters $m_{\mathrm{c},i}$, $m_{\mathrm{s},i}$ and the resulting harmonic components $k_{\mathrm{s},i}$, $k_{\mathrm{c},i}$ in the CT, which are obtained by a Fourier decomposition, are conveniently expressed as

$$\mathbf{m} = \begin{bmatrix} m_{\mathrm{c},1} & m_{\mathrm{s},1} & \dots & m_{\mathrm{c,n}} & m_{\mathrm{s,n}} \end{bmatrix}^{\mathrm{T}} \tag{10}$$

and

$$\mathbf{k} = \begin{bmatrix} k_{\mathrm{s},i} & k_{\mathrm{c},i} & \dots & k_{\mathrm{s},m} & k_{\mathrm{c},m} \end{bmatrix}^{\mathrm{T}}\,. \tag{11}$$

As shown by the above analytical derivation, the air gap modulation is an adequate tool for shaping the CT towards a desired shape [34]. Since stators of electric machines are typically made of laminated electrical steel and the individual steel sheets are either laser cut (in a prototyping stage) or punched (in mass production), the optimized stator shape does not create a significant additional production effort.

B. Optimization Algorithm

The optimization is initialized with a design based on the findings obtained in the analysis of the generic flux modulator, which is depicted in Fig. 8a and parameterized in Table I. Following design choices were made prior to the presented optimization:

- For the practical realization, the stator teeth should be shaped straight, such that coil formers can be used to pre-confection the windings.
- The analysis of Sec. III-A requires sinusoidal PM remanent flux density, however, this was approximated with a gap between two PMs $\beta_{\mathrm{PMgap}} = 50^{\mathrm{o}}$ and constant remanent flux density therein. Consequently, higher utilization of magnet material is achieved.

The flowchart describing the CT shaping optimization algorithm is given in Fig. 7. After the initialization with a start geometry (cf. Fig. 8a), CT $T_{\mathrm{cog,gen}}$ is computed with 2-D FEM simulations as function of the angle of rotational position θ.

Similarly, the CT target T^*_{cog}, which is $-T_{\mathrm{cog,harv}}$ in the presented application (cf. (1)) can be decomposed and expressed in terms of a vector $\mathbf{k}^*$. Conveniently, the difference (residual) between the CT at the current iteration step and the CT target can be written as

$$\mathbf{k}_{\mathrm{res}} = \mathbf{k}^* - \mathbf{k}_i\,. \tag{12}$$

The utilized algorithm iterates the geometry and is terminated when the residual is sufficiently small $\mathrm{norm}(\mathbf{k}_{\mathrm{res}}) < \epsilon$, as a complete vanishing of it cannot be reached due to the

Copyright (c) 2017 IEEE. Personal use is permitted. For any other purposes, permission must be obtained from the IEEE by emailing pubs-permissions@ieee.org.

This is the author's version of an article that has been published in this journal. Changes were made to this version by the publisher prior to publication.
The final version of record is available at http://dx.doi.org/10.1109/TIE.2017.2733441

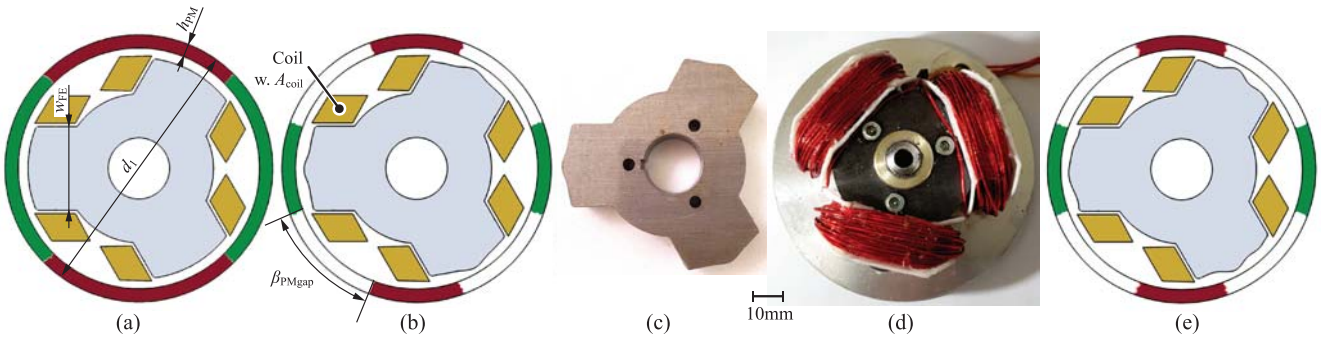

Fig. 8. Outrunner generator geometries. (a) Initial geometry fed into the optimization, (b) resulting optimized stator geometry with sinusoidal CT , (c) a photograph of the prototype stator. (d) The stator with winding system. (e) The resulting stator geometry optimized for minimal CT.

TABLE I
PARAMETERS USED FOR THE 2-D FEM SIMULATIONS OF THE GENERATOR.

Parameter	Variable	Value
Generator bore diameter	d_1	70 mm
PM height	h_{PM}	3.5 mm
2-D rotor diameter[a]	$d_{\mathrm{rot,Aeq}}$	120 mm
Actual rotor diameter	d_{rot}	77 mm
Stator material		M235-35A
Stator rel. permeability	$\mu_{\mathrm{sat,rel}}$	1000
Rotor rel. permeability	$\mu_{\mathrm{rot,rel}}$	700
Stator width	l_{y}	12 mm
Number of pole pairs	p	2
Number of phases	m	3
Nominal air gap	g_0	2.5 mm
PM grade		N48M
PM remanent flux density	B_{rem}	1.4 T
PM rel. permeability	$\mu_{\mathrm{PM,rel}}$	1.05
Stator tooth width	w_{FE}	22 mm
Coil cross section	A_{coil}	76 mm^2

[a] Used to represent the actually pot-shaped rotor flux path in 2-D simulation.

numerical nature of simulations. In the following optimization procedure, $\epsilon = 5\,\mathrm{Nmm}$ ($< 5\%$ of the CT target) is selected as it leads to a sufficient reduction of the total CT.

The update of geometry parameters is a multi-dimensional Secant Method, which is related to the multi-dimensional Newton-Raphson Method [35], but utilizes the secant as an approximation for the Jacobian matrix,

$$\frac{\partial \mathbf{k}}{\partial \mathbf{m}} \approx \tilde{\mathbf{J}} = \begin{bmatrix} \frac{\Delta k_{\mathrm{s},1}}{\Delta m_{\mathrm{c},1}} & \cdots & \frac{\Delta k_{\mathrm{s},1}}{\Delta m_{\mathrm{s,n}}} \\ \vdots & \ddots & \vdots \\ \frac{\Delta k_{\mathrm{c,m}}}{\Delta m_{\mathrm{c},1}} & \cdots & \frac{k_{\mathrm{c,m}}}{m_{\mathrm{s,n}}} \end{bmatrix}, \tag{13}$$

for finding the root (zero) of the error function ($\mathbf{k}_{\mathrm{res}}$ here) [36]. For obtaining e.g. the first column in $\tilde{\mathbf{J}}$, the parameter $m_{\mathrm{c},1}$ is perturbed and a simulation is conducted. The difference in terms of CT decomposition $\mathbf{k}$ yields the values for the first column. This procedure is conducted for all elements of the geometry parameter vector, such that $\tilde{\mathbf{J}}$ can be filled.

Then, the geometry parameter $\mathbf{m}$ is updated such that the torque residual $\mathbf{k}_{\mathrm{rem}}$ is reduced,

$$\mathbf{m}_{i+1} = \mathbf{m}_i - d_{\mathrm{damping}}\, \tilde{\mathbf{J}}^{+}\, \mathbf{k}_{\mathrm{res}}\ . \tag{14}$$

The pseudoinverse of the approximated Jacobian matrix,

$$\tilde{\mathbf{J}}^{+} := \left(\tilde{\mathbf{J}}^{\mathrm{T}}\tilde{\mathbf{J}}\right)^{-1}\tilde{\mathbf{J}}^{\mathrm{T}}\ ,$$

is used for the update step since the existence of $\tilde{\mathbf{J}}^{-1}$ cannot be guaranteed. Due to the strong nonlinearity of the optimization problem, a damping factor d_{damping} is applied in the update step; $d_{\mathrm{damping}} = 0.2$ showed good convergence.

IV. RESULTS

A. Simulation Results

CT optimization is conducted for the presented three-phase outrunner generator with the initial geometry of Fig. 8a. For the application example, the goal of shaping the CT is to reduce the start-up speed of the presented EEH. As Fig. 4 shows, the EEH CT cannot be compensated for all operating points (OPs), since it varies over air gap. Therefore, the optimization goal is to achieve a sinusoidal generator CT with amplitude of $100\,\mathrm{Nmm}$.

After a first, coarse optimization, the geometry obtained by 2-D simulation was analyzed in a 3-D simulation as it was expected that 2-D FEM overestimates the CT amplitude (cf. CT results in Fig. 9). This is due to the aspect ratio of the generator as the rather short axial length ($12\,\mathrm{mm}$) compared to the diameter ($70\,\mathrm{mm}$) can lead to axial fringing field. Namely, the magnetic flux density in the air gap is smaller towards the axial ends of the machine, compared to symmetry plane in the axial middle. Accordingly, simulations showed that the CT amplitude obtained by 3-D FEM is only 70% of the value predicted by 2-D FEM. However, the shape of the CT curve remains almost identical. Therefore, and due to the fact that 3-D simulations turned out to be computationally too expensive for CT optimizations, the target amplitude for the 2-D optimization was increased to $\hat{T}^* = 100\,\mathrm{Nmm}/0.7 = 143\,\mathrm{Nmm}$.

Moreover, an optimization for vanishing CT was conducted, whose sole purpose is to demonstrate the capability of the presented algorithm further. The initial geometry (cf. Fig. 8a) remains the same, but the CT target is set to zero $\hat{T}^* = 0\,\mathrm{Nmm}$.

Fig. 8b shows the obtained geometry with $\hat{T}^* = 143\,\mathrm{Nmm}$, together with a photograph of the hardware realization in

Copyright (c) 2017 IEEE. Personal use is permitted. For any other purposes, permission must be obtained from the IEEE by emailing pubs-permissions@ieee.org.

This is the author's version of an article that has been published in this journal. Changes were made to this version by the publisher prior to publication.
The final version of record is available at http://dx.doi.org/10.1109/TIE.2017.2733441

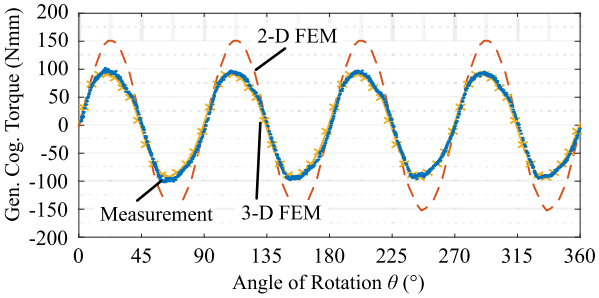

Fig. 9. Generator CT measurement and FEM simulation results. 3-D FEM simulations are agreeing well with measurements, while 2-D FEM simulations overestimate the torque due to the fringing field of this axially short ($12\,\mathrm{mm}$) machine compared to the diameter ($70\,\mathrm{mm}$). The torque shape remains identical, which still justifies utilizing 2-D FEM for CT shape optimization.

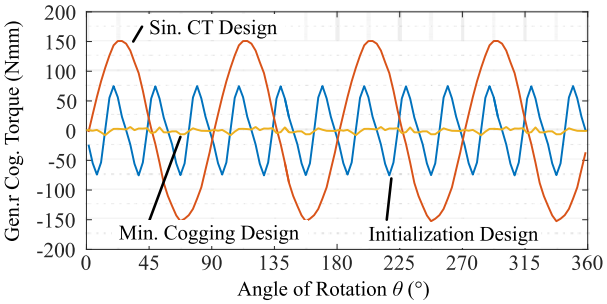

Fig. 10. CT waveforms prior and after the conducted optimization obtained by 2-D FEM simulation. The curve entitled "initialization design" is the CT of Fig. 8a and shows the CT prior to optimization, curve "min. cogging design" shows the CT of Fig. 8d. The curve "sin. CT design" shows the optimization result for the application with the EEH and as targeted a sinusoidal CT shape; the geometry is depicted in Fig. 8b.

Fig. 8c. Fig. 8d shows the stator mounted on a base plate with windings. Fig. 8e shows the optimized geometry for minimal CT. Furthermore, the geometry parameter vector $\mathbf{m}$ for the optimized geometries is given in Table II.

TABLE II
AIR GAP MODULATION PARAMETERS.

Variable	Init. Val.	Sin. CT Pattern	Min. CT
$m_{\mathrm{c},1}$	0	0.1884	0.0063
$m_{\mathrm{s},1}$	0	0.0456	0.0003
$m_{\mathrm{c},2}$	0	0.0100	0.0162
$m_{\mathrm{s},2}$	0	0.0028	0.0055
$m_{\mathrm{c},3}$	0	−0.2305	-0.2272
$m_{\mathrm{s},3}$	0	0.0032	0.0021
$m_{\mathrm{c},4}$	0	0.0011	-0.0110
$m_{\mathrm{s},4}$	0	0.0033	0.0031
$m_{\mathrm{c},5}$	0	−0.0072	0.1169
$m_{\mathrm{s},5}$	0	0.0129	0.0491
$m_{\mathrm{c},6}$	0	−0.0640	-0.0599
$m_{\mathrm{m},6}$	0	0.0042	0.0036
$m_{\mathrm{i}>6}$	0	0	0

CT simulation results for the initial geometry and the two optimized geometries are depicted in Fig. 10. It clearly shows that the conducted approach is capable of optimizing the CT towards a special shape as desired for the application example of the EEH. Moreover, the applied technique can be utilized for eliminating the CT of axially short electric machines (e.g. in direct drive systems), where skewing is not feasible.

Furthermore, simulation results concerning the stator iron losses shall be briefly discussed as a non-uniform air gap might lead to partially increased flux density. Iron losses P_{Fe} in laminated iron are due to hysteresis losses and eddy-current losses as discussed (and separated) in [37]. However, for this analysis the iron losses are calculated based on the Steinmetz equation for the material M235-35A (cf. EN 10106; with $0.35\,\mathrm{mm}$ lamination thickness), as

$$P_{\mathrm{Fe}} = \frac{l_{\mathrm{y}}}{1\,\mathrm{m}} \int_{A_{\mathrm{stat.}}} 46\,\frac{\mathrm{W}}{\mathrm{m}^3} \left(\frac{f_{\mathrm{el}}}{1\,\mathrm{Hz}}\right)^{1.3} \left(\frac{B_{\mathrm{pk}}(A)}{1\,\mathrm{T}}\right)^{1.9} \mathrm{dA}, \quad (15)$$

where the peak flux density B_{pk} of every point in the stator during one electrical period is extracted from 2-D FEM simulations. A map of peak flux density for the optimized generator with sinusoidally shaped CT is shown in Fig. 11 and one can see that partial saturation occurs only on the edges of the stator. Finally, for the nominal OP, listed in Table III, total stator iron losses of $P_{\mathrm{stator,FE}} = 0.1\,\mathrm{W}$ were calculated, showing that the presented approach is not particularly prone to unjustifiably high stator iron losses.

B. Cogging Torque Measurement & EEH Start-up Speed

The optimized, laminated stator according to Fig. 8c and Fig. 8d was built and assembled with the phase windings, which were pre-manufactured on a 3-D printed coil formers with $0.8\,\mathrm{mm}$ wall thickness. CT measurements and FEM simulation results are shown in Fig. 9. As previously discussed, the 2-D simulation overestimates the CT by 30% (which was already included in the optimization target). On the other hand, the 3-D FEM simulation predicts the measurements with high accuracy. Therefore, it can be concluded that the presented

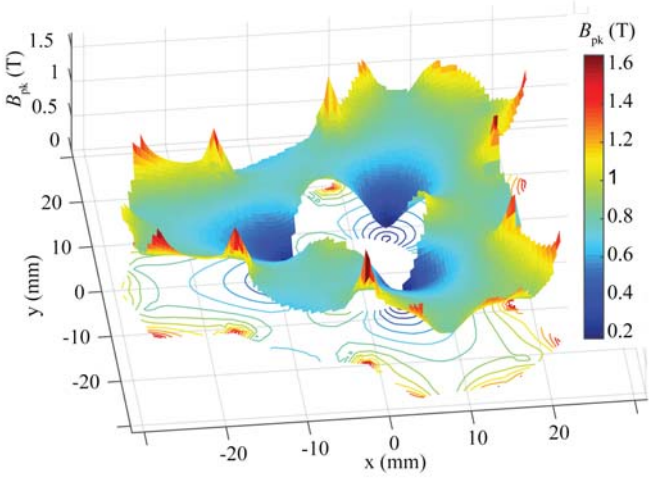

Fig. 11. Map of peak flux density in the stator obtained by 2-D FEM simulation and utilized to compute the stator iron losses.

Copyright (c) 2017 IEEE. Personal use is permitted. For any other purposes, permission must be obtained from the IEEE by emailing pubs-permissions@ieee.org.

This is the author's version of an article that has been published in this journal. Changes were made to this version by the publisher prior to publication.
The final version of record is available at http://dx.doi.org/10.1109/TIE.2017.2733441

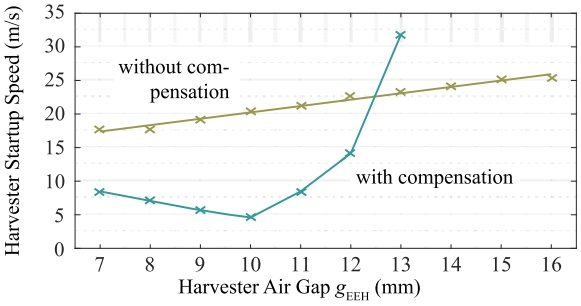

Fig. 12. Measurement results of system start-up speed without compensation (EEH only) and with the proposed CT compensation due to the specially shaped stator of the generator.

concept is not particularly prone to manufacturing tolerances on the stator as well as on the magnets.

The EEH and the optimized generator were assembled and aligned in an angle such that CT curves of Fig. 4 and Fig. 9 compensate each other, which results in a highly reduced overall CT of the system: EEH and generator. The main benefit of the conducted approach for the application example with the EEH can be found in Fig. 12. Clearly, the goal of reducing the harvester's start-up speed is achieved. For smaller air gaps (8 mm), the EEH CT is under-compensated, while for larger air gaps (12 mm) an overcompensation occurs. In addition, for an air gap of 13 mm and larger, the CT imposed by the generator has a negative effect on the start-up speed. However, this is not of practical relevance for the presented harvester as also the output power vanishes (cf. Fig. 2). As previously discussed, it is not possible to compensate the EEH CT for the whole air gap range of 8...12 mm, where the harvester is intended to be used, however, for the specified range a significant reduction of the start-up speed is achieved. It should be remarked that no direct measurement of the remaining CT is possible as harvester and generator form a compact unit without an accessible shaft.

Overall, measurements in Fig. 12 show that the introduced principle of CT compensation (cf. (1)) and the applied stator geometry optimization algorithm (cf. Sec. III-B) for a desired CT shape lead to successful results in the described application. In contrast to the CT shaping methods presented in literature, the described approach allows to optimize the CT of an electric machine towards any shape in an iterative manner.

C. Generator Performance

The electrical performance of the generator, whose CT is optimized in Sec. IV, concludes the analysis conducted in this work and will be discussed briefly in the following.

The electrical characteristics of the generator and its performance figures for the EEH maximum power point (MPP) at $g_{\mathrm{EEH}} = 8\,\mathrm{mm}$ are shown. Electrical output power measurements are plotted in Fig. 13 and are proving the harvesting capabilities, $P_{\mathrm{out}} > 12\,\mathrm{W}$ of the harvester unit. For the presented measurement, the generator was loaded with a three-phase resistor, whose resistance was decreased until the MPP was found. The output power measurement indicates an

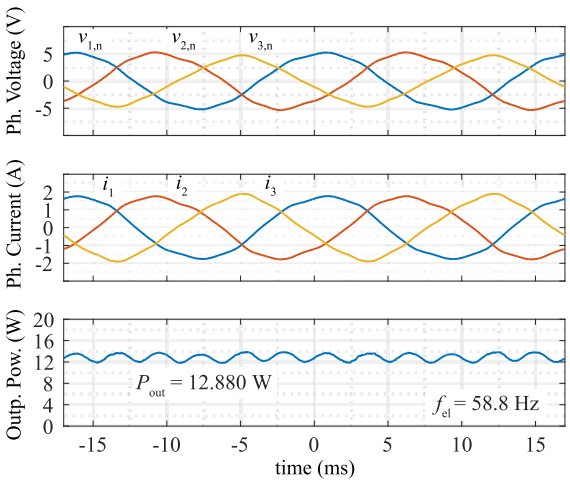

Fig. 13. Output power measurement at $g_{\mathrm{EEH}} = 8\,\mathrm{mm}$ and $v_{\mathrm{MES}} = 22.2\,\mathrm{m/s}$. The generator was loaded with a three-phase resistor and measurements are for the maximum power point of the system.

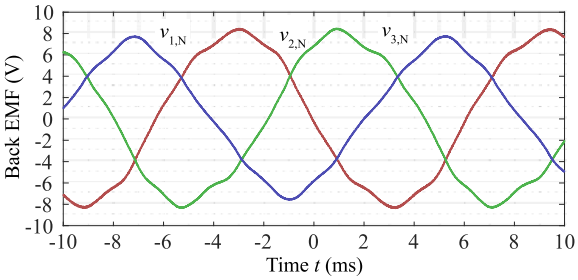

Fig. 14. Back EMF measurement of the generator for the rotational frequency $\omega_{\mathrm{EEH}} = 250\,\mathrm{rad/s}$.

acceptably small power ripple of $< 8\%$ (peak-peak). The back EMF measurement in Fig. 14 show that the air gap modulation causes certain -but acceptable- asymmetry, given the well increased utility in the described application. Moreover, copper losses were calculated as $P_{\mathrm{cu}} = 1.8\,\mathrm{W}$ for this OP.

In a further investigation, losses in the bearings were analyzed. Measurements of the bearing friction torque, which were conducted with a high precision torque sensor, are depicted in Fig. 15. Indeed, it was concluded that the bearing losses in the MPP, $P_{\mathrm{bearing}} = 2.8\,\mathrm{W}$, are a significant loss component. The bearing losses could potentially be decreased with smaller bearings in the considered system. This was not implemented for the built prototype as it causes a lower limit on air gap g_{EEH} for measurements due to axial pull. On the other hand, the goal of the prototype system was to conduct measurements across a wide parameter range. Furthermore, rotor eddy current losses were estimated as $P_{\mathrm{rot}} > 1\,\mathrm{W}$ with the rotor, currently made of solid S235 construction steel. Laminating the pot-shaped rotor can clearly reduce this loss component, but was not implemented in the built prototype system as it would have complicated the mechanical design and would have rendered it prone to unbalance.

Copyright (c) 2017 IEEE. Personal use is permitted. For any other purposes, permission must be obtained from the IEEE by emailing pubs-permissions@ieee.org.

This is the author's version of an article that has been published in this journal. Changes were made to this version by the publisher prior to publication.
The final version of record is available at http://dx.doi.org/10.1109/TIE.2017.2733441

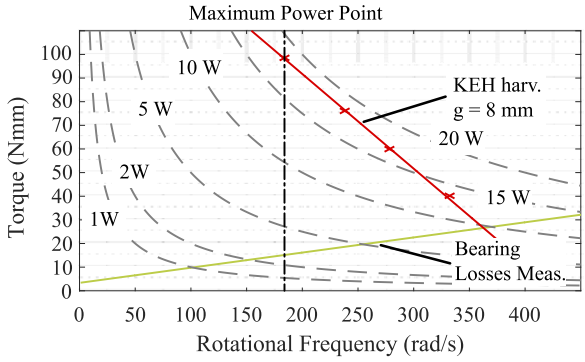

Fig. 15. Losses in bearings, obtained by measurements with the precision torque sensor. Additionally, the torque supplied by the EEH and the maximum power point therefore are shown.

TABLE III
GENERATOR CHARACTERISTICS.

Parameter	Variable	Value
Nominal torque	T_n	100 Nmm
Nominal speed	n_n	1764 rpm
Nominal mechanical power	P_mech	18 W
No. of pole pairs	p	2
Coil cross section	A_coil	76 mm^2
Number of turns	N	87
Achieved copper filling factor	k_cu	0.48
Stator iron losses	P_Fe	0.1 W
Copper losses	P_Cu	1.8 W

V. CONCLUSION

This paper describes a method for optimizing the cogging torque (CT) of a permanent magnet (PM) machine towards a desired shape. In a given application example, the described algorithm is applied to a PM outrunner generator, which is integrated with an electromechanical energy harvester (EEH, [20]) in a compact unit. The generator's CT is shaped such that the naturally present CT of the EEH is highly reduced in the desired operating range ($g_\mathrm{EEH} = 8...12\,\mathrm{mm}$). This leads to the, otherwise not achievable, starting capability of the energy harvester unit at low speeds as verified with measurements.

The CT simulations for the optimization are conducted with 2-D FEM and a harmonic decomposition, similar to a Fourier decomposition, is computed. A presented algorithm, whose influence on the machine geometry is a vector of air gap modulation parameters, optimizes the machine's geometry until the desired CT shape is achieved. In contrast to the CT minimization methods presented in literature, the described approach allows to optimize the CT of an electric machine towards any shape in an iterative manner.

Besides the presented design for the application example, which shows sinusoidal CT of rather large magnitude (100 Nmm), a further design example is presented, where the algorithm is utilized for an optimization aiming for vanishing CT. This clearly shows that the conducted approach is valuable for CT optimizations for a variety of applications. It could be utilized to compensate an externally triggered undesired torque or power ripple (e.g. originating from a prime mover or a mechanical load system: generators, which are directly coupled to a prime mover or machines directly coupled to a piston compressor) by specially shaping the CT as conducted in the considered application example, or be utilized for eliminating the CT of axially short electric machines (e.g. in direct drive systems), where skewing is not feasible.

ACKNOWLEDGMENT

The authors would like to express their sincere appreciation to Nabtesco Corp., Japan, for the financial and technical support of research on energy harvesting technologies at the Power Electronic Systems Laboratory, ETH Zurich, which provided the basis for achieving the results presented in this paper. In particular, inspiring technical discussions with K. Nakamura, Y. Tsukada and Y. Ono are acknowledged.

REFERENCES

[1] D. Wang, X. Wang, and S. Y. Jung, "Cogging torque minimization and torque ripple suppression in surface-mounted permanent magnet synchronous machines using different magnet widths," *IEEE Trans. Magn.*, vol. 49, no. 5, pp. 2295–2298, May. 2013.
[2] N. Chen, S. L. Ho, and W. N. Fu, "Optimization of permanent magnet surface shapes of electric motors for minimization of cogging torque using FEM," *IEEE Trans. Magn.*, vol. 46, no. 6, pp. 2478–2481, Jun. 2010.
[3] S. H. Lee, Y. J. Kim, K. S. Lee, and S. J. Kim, "Multiobjective optimization design of small-scale wind power generator with outer rotor based on box-behnken design," *IEEE Trans. Appl. Supercond.*, vol. 26, no. 4, pp. 1–5, Jun. 2016.
[4] M. Lukaniszyn, M. JagieLa, and R. Wrobel, "Optimization of permanent magnet shape for minimum cogging torque using a genetic algorithm," *IEEE Trans. Magn.*, vol. 40, no. 2, pp. 1228–1231, Mar. 2004.
[5] A. N. Patel, "Cogging torque minimization by magnet edge inset variation technique in radial flux surface mounted permanent magnet brushless DC (PMBLDC) motor," in *Proc. NUiCONE*, pp. 1–4, Nov. 2015.
[6] I. Petrov, P. Ponomarev, Y. Alexandrova, and J. Pyrhönen, "Unequal teeth widths for torque ripple reduction in permanent magnet synchronous machines with fractional-slot non-overlapping windings," *IEEE Trans. Magn.*, vol. 51, no. 2, pp. 1–9, Feb. 2015.
[7] S. Jurkovic, K. Rahman, B. Bae, N. Patel, and P. Savagian, "Next generation Chevy Volt electric machines; design, optimization and control for performance and rare-earth mitigation," in *Proc. IEEE ECCE USA*, pp. 5219–5226, Sep. 2015.
[8] G. Zhao, W. Hua, X. Zhu, and G. Zhang, "The influence of dummy slots on stator surface-mounted permanent magnet machines," *IEEE Trans. Magn.*, Jan. 2017.
[9] B. Li, J. Zhao, X. Liu, Y. Guo, H. Hu, and J. Li, "Detent force reduction of an arc-linear permanent magnet synchronous motor by using compensation windings," *IEEE Trans. Ind. Electron.*, Dec. 2016.
[10] R. Lateb, N. Takorabet, and F. Meibody-Tabar, "Effect of magnet segmentation on the cogging torque in surface-mounted permanent-magnet motors," *IEEE Trans. Magn.*, vol. 42, no. 3, pp. 442–445, Mar. 2006.
[11] W. Zhao, T. A. Lipo, and B. I. Kwon, "Torque pulsation minimization in spoke-type interior permanent magnet motors with skewing and sinusoidal permanent magnet configurations," *IEEE Trans. Magn.*, vol. 51, no. 11, pp. 1–4, Nov. 2015.
[12] Z. Q. Zhu and D. Howe, "Influence of design parameters on cogging torque in permanent magnet machines," *IEEE Trans. Ene. Conv.*, vol. 15, no. 4, pp. 407–412, Dec. 2000.
[13] M. G. Angle, J. H. Lang, J. L. Kirtley, S. Kim, and D. Otten, "Cogging torque reduction in permanent-magnet synchronous machines with skew," in *Proc. IEEE ICEM*, pp. 207–211, Sep. 2016.
[14] J. Wang, R. Qu, Y. Tang, Y. Liu, B. Zhang, J. He, Z. Zhu, H. Fang, and L. Su, "Design of a superconducting synchronous generator with LTS field windings for 12 MW offshore direct-drive wind turbines," *IEEE Trans. Ind. Electron.*, vol. 63, no. 3, pp. 1618–1628, Mar. 2016.
[15] M. S. Islam, S. Mir, and T. Sebastian, "Issues in reducing the cogging torque of mass-produced permanent-magnet brushless DC motor," *IEEE Trans. Ind. Appl.*, vol. 40, no. 3, pp. 813–820, May 2004.

Copyright (c) 2017 IEEE. Personal use is permitted. For any other purposes, permission must be obtained from the IEEE by emailing pubs-permissions@ieee.org.

This is the author's version of an article that has been published in this journal. Changes were made to this version by the publisher prior to publication.
The final version of record is available at http://dx.doi.org/10.1109/TIE.2017.2733441

[16] D. G. Dorrell, M. F. Hsieh, M. Popescu, L. Evans, D. A. Staton, and V. Grout, "A review of the design issues and techniques for radial-flux brushless surface and internal rare-earth permanent-magnet motors," *IEEE Trans. Ind. Electron.*, vol. 58, no. 9, pp. 3741–3757, Sep. 2011.
[17] C. Studer, A. Keyhani, T. Sebastian, and S. K. Murthy, "Study of cogging torque in permanent magnet machines," in *Proc. IEEE Ind. Appl. Conf.*, vol. 1, pp. 42–49 vol.1, Oct. 1997.
[18] M. Johnson, "High torque stepping motor," U.S. Patent 4 127 802, Nov. 28, 1978.
[19] J. Bacher and G. Maier, "Actions to increase the cogging torque and effects of the increased cogging torque to permanent magnet dc motors," *Proc. Power Electr. and Appl. Conf. (EPE)*, Sep. 2005.
[20] M. Flankl, A. Tüysüz, I. Subotic, and J. W. Kolar, "Novel contactless axial-flux permanent-magnet electromechanical energy harvester," in *Proc. IEEE APEC Expo.*, pp. 623–630, Mar. 2016.
[21] M. Flankl, A. Tüysüz, and J. W. Kolar, "Outrunner generator with optimized cogging torque pattern for an electromechanical energy harvester," in *Proc. 42nd Annu. IEEE IECON*, pp. 4293–4300, Oct. 2016.
[22] M. Flankl, A. Tüysüz, and J. W. Kolar, "Analysis of a watt-range contactless electromechanical energy harvester facing a moving conductive surface," in *Proc. IEEE ECCE USA*, pp. 414–420, Sep. 2015.
[23] European Committee for Standardization, *Steels for quenching and tempering*, Std. EN 10 083-1:2006, 2006.
[24] A. Tüysüz, A. Looser, J. W. Kolar, and C. Zwyssig, "Novel miniature motors with lateral stator for a wide torque and speed range," in *Proc. 36th Annu. IEEE IECON*, pp. 1741–1747, Nov. 2010.
[25] A. Tüysüz, "Novel Miniature Motors for Wide Speed and Torque Ranges," Ph.D. dissertation, ETH Zurich, 2014.
[26] E. Favre, L. Cardoletti, and M. Jufer, "Permanent-magnet synchronous motors: A comprehensive approach to cogging torque suppression," *IEEE Trans. Ind. Appl.*, vol. 29, no. 6, pp. 1141–1149, Nov. 1993.
[27] Y. Zhang and J. Zhu, "A novel duty cycle control strategy to reduce both torque and flux ripples for dtc of permanent magnet synchronous motor drives with switching frequency reduction," *IEEE Trans. Power Electron.*, vol. 26, no. 10, pp. 3055–3067, Oct. 2011.
[28] A. Mora, A. Orellana, J. Juliet, and R. Cardenas, "Model predictive torque control for torque ripple compensation in variable-speed pmsms," *IEEE Trans. Ind. Electron.*, vol. 63, no. 7, pp. 4584–4592, Jul. 2016.
[29] G. Feng, C. Lai, and N. Kar, "A closed-loop fuzzy logic based current controller for pmsm torque ripple minimization using the magnitude of speed harmonic as the feedback control signal," *IEEE Trans. Ind. Electron.*, Nov. 2016.
[30] G. Bramerdorfer, W. Amrhein, and S. Lanser, "PMSM for high demands on low torque ripple using optimized stator phase currents controlled by an iterative learning control algorithm," in *Proc. 39th Annu. IEEE IECON*, pp. 8488–8493, Nov. 2013.
[31] W. Wu, "Disturbance compensation for DC motor mechanism low speed regulation: a feedforward and feedback implementation," in *Proc. IEEE Conf. on Decis. Contr. and Europ. Contr. Conf.*, pp. 1614–1619, Dec. 2011.
[32] H. Chu, B. Gao, W. Gu, and H. Chen, "Low speed control for permanent magnet DC torque motor using observer-based nonlinear triple-step controller," *IEEE Trans. Ind. Electron.*, Aug. 2016.
[33] M. Flankl, A. Tüysüz, and J. W. Kolar, "Analysis and power scaling of a single-sided linear induction machine for energy harvesting," in *Proc. 41st Annu. IEEE IECON*, pp. 835–842, Nov. 2015.
[34] S. U. Chung, S. H. Moon, D. J. Kim, and J. M. Kim, "Development of a 20-pole 24-slot SPMSM with consequent pole rotor for in-wheel direct drive," *IEEE Trans. Ind. Electron.*, vol. 63, no. 1, pp. 302–309, Jan. 2016.
[35] V. S. Ryaben'kii and S. V. Tsynkov, *A theoretical introduction to numerical analysis*. CRC Press, 2007.
[36] M. Hanke-Bourgeois, *Grundlagen der Numerischen Mathematik und des Wissenschaftlichen Rechnens (in German)*. Vieweg+Teubner, 2009.
[37] A. Boglietti, A. Cavagnino, D. M. Ionel, M. Popescu, D. A. Staton, and S. Vaschetto, "A general model to predict the iron losses in PWM inverter-fed induction motors," *IEEE Trans. Ind. Appl.*, vol. 46, no. 5, pp. 1882–1890, Sep. 2010.

Michael Flankl (S'12) received his BSc degree in Mechatronics from JKU Linz, Austria in 2012. He has received the MSc degree in Robotics, Systems & Control from ETH Zurich, Switzerland in 2014. Since May 2014, he is a PhD candidate at the Power Electronic Systems Laboratory at ETH Zurich, Switzerland. He is supervised by Prof. Johann W. Kolar and working on mechatronic energy harvesting solutions. His further areas of interest include electric transportation and drive systems.

Arda Tüysüz (S'10 - M'13) received his B.Sc. degree in electrical engineering from Istanbul Technical University, Istanbul, Turkey, in 2006, his M.Sc. degree in electrical power engineering from RWTH Aachen University, Aachen, Germany, in 2009, and his Ph.D. degree in electrical drives from the Swiss Federal Institute of Technology (ETH) Zurich, Zurich, Switzerland, in 2015. He is currently a Post-Doctoral Researcher with the Power Electronic Systems Laboratory of ETH Zurich. His research interests include novel electrical machine topologies, self-sensing control of high-speed electrical machines, electrical drives with very high signal-to-noise ratio and wide-bandgap power devices for very efficient and compact electrical drive systems.

Johann W. Kolar (M'89-SM'04-F'10) is a Fellow of the IEEE and has received his M.Sc. degree in Industrial Electronics and Control Engineering and his Ph.D. degree in Electrical Engineering (summa cum laude) from the Vienna University of Technology, Austria. Since 1984 he has been working as an independent researcher and international consultant in close collaboration with the Vienna University of Technology, in the fields of power electronics, industrial electronics and high performance drives. He was appointed Assoc. Professor and Head of the Power Electronic Systems Laboratory at the Swiss Federal Institute of Technology (ETH) Zurich on Feb. 1, 2001, and was promoted to the rank of Full Prof. in 2004. He has proposed numerous novel PWM converter topologies (e.g. the VIENNA Rectifier, Sparse Matrix Converter, and SWISS Rectifier), and modulation and control concepts and has supervised over 60 Ph.D. students. He has published over 750 scientific papers in international journals and conference proceedings, 3 book chapters, and has filed more than 140 patents. He has presented over 20 educational seminars at leading international conferences, has served as IEEE PELS Distinguished Lecturer from 2012 through 2016, and has received 25 IEEE Transactions and Conference Prize Paper Awards, the 2014 IEEE Power Electronics Society R. David Middlebrook Achievement Award, the 2014 SEMIKRON Innovation Award, the 2016 IEEE William E. Newell Power Electronics Award, the 2016 IEEE PEMC Council Award, and the ETH Zurich Golden Owl Award for excellence in teaching. He has initiated and/or is the founder of 4 ETH Spin-off companies. The focus of his current research is on ultra-compact and ultra-efficient SiC and GaN converter systems, wireless power transfer, Solid-State Transformers, Power Supplies on Chip, as well as ultra-high speed and ultra-light weight drives, bearingless motors, and energy harvesting.

Copyright (c) 2017 IEEE. Personal use is permitted. For any other purposes, permission must be obtained from the IEEE by emailing pubs-permissions@ieee.org.